A Geometry-Based Stochastic Model for Wideband MIMO Mobile-to-Mobile Channels

Xiang Cheng[†], Cheng-Xiang Wang[†], and David I. Laurenson[††]

[†]Joint Research Institute for Signal and Image Processing, Heriot-Watt University, EH14 4AS, Edinburgh, UK.

[††]Joint Research Institute for Signal and Image Processing, University of Edinburgh, EH9 3JL, Edinburgh, UK.

Email: xc48@hw.ac.uk, cheng-xiang.wang@hw.ac.uk, dave.laurenson@ed.ac.uk

***Abstract*—In this paper, based on the tapped delay line (TDL) structure, we propose a geometry-based stochastic model (GBSM) for wideband multiple-input multiple-output (MIMO) mobile-to-mobile (M2M) Ricean fading channels. The proposed wideband model is the first GBSM that has the ability to study the impact of the vehicular traffic density (VTD) on channel statistics for different time delays, i.e., for every tap in our model. From the proposed model, the space-time (ST) correlation function (CF) and the corresponding space-Doppler (SD) power spectral density (PSD) are derived. Excellent agreement is achieved between the theoretical Doppler PSDs and measured data, demonstrating the utility of the proposed model.**

I. Introduction

In recent years, M2M communications have received increasing attention due to some new applications, such as wireless mobile ad hoc networks, relay-based cellular networks, and dedicated short range communications for intelligent transportation systems (IEEE 802.11p). Such M2M systems consider that both the transmitter (Tx) and receiver (Rx) are in motion and equipped with low elevation antennas. To practically analyze and design M2M systems, it is necessary to have reliable knowledge of the propagation channel and the corresponding realistic channel model [1]. Akki and Haber [2], [3] were the first to propose a GBSM for two-dimensional (2D) isotropic single-input single-output (SISO) M2M Rayleigh fading channels. In [4], a 2D GBSM considering only double-bounced rays was presented for non-isotropic MIMO M2M Rayleigh fading channels. In [5], the authors proposed a general 2D GBSM with both single- and double-bounced rays for non-isotropic MIMO M2M Ricean fading channels. The 2D model in [5] was further extended to a 3D model in [6]. More recently, in [7]–[9], we proposed 2D GBSMs that for the first time, have the ability to study the impact of the VTD on channel statistics.

However, all the above mentioned GBSMs are narrowband M2M channel models. Most potential transmission schemes for M2M communications use relatively wide bandwidths (e.g., approximately 10 MHz for the IEEE 802.11p standard). The underlying M2M channels present frequency selectivity since the signal bandwidth is larger than the coherence bandwidth of such channels (normally around 2 MHz [10]). To the best of the authors' knowledge, only [11] proposed a 3D GBSM for wideband MIMO M2M Ricean fading channels. However, the model cannot describe the channel statistics for different time delays, which are important for M2M channels as mentioned in [12] and [13]. Although the measurement campaign in [10] has demonstrated that the VTD significantly affects the channel statistics for M2M channels, the impact of the VTD is not considered in the wideband model in [11].

To fill the above gap, through the application of the TDL concept, we propose a new wideband GBSM which is an extension of our model in [8] with respect to the frequency-selectivity. This wideband model comprises a two-ring model and a multiple confocal ellipses model considering both single- and double-bounced rays. By using the multiple confocal ellipses to construct a TDL structure, the proposed wideband model can investigate the channel statistics for different time delays, i.e., per-tap channel statistics. In order to take into account the impact of the VTD on channel statistics for every tap in the proposed wideband model, while retaining its complexity similar to that of our narrowband model in [8], we first distinguish between the moving and stationary scatterers, which are described by a two-ring model and a multiple confocal ellipses model, respectively. Then from the analysis of real environments of M2M communications, we generate a novel and simple approach to incorporate the impact of the VTD into every tap of our wideband model. From the proposed model, we derive the ST CF and the corresponding SD PSD. Finally, the obtained theoretical Doppler PSDs and measurement data in [13] are compared. Excellent agreement between them demonstrates the utility of the proposed model.

II. A New Wideband MIMO M2M GBSM

Let us now consider a wideband MIMO M2M communication system with M_T transmit and M_R receive omni-directional antenna elements. Both the Tx and Rx are equipped with low elevation antennas. Fig. 1 illustrates the geometry of the proposed GBSM, which is the combination of a two-ring model and a multiple confocal ellipses model considering both single- and double-bounced rays, as well as the line-of-sight (LoS) components. Note that in Fig. 1, we used uniform linear antenna arrays with $M_T = M_R = 2$ as an example. The proposed model is applicable to MIMO systems with an arbitrary number of antenna elements. The two-ring model defines two rings of effective scatterers, one around the Tx and the other around the Rx. Suppose there are $N_{1,1}$ effective scatterers around the Tx lying on a ring of radius R_T and the $n_{1,1}$th ($n_{1,1}$=1, ..., $N_{1,1}$) effective scatterer is denoted by $s^{(n_{1,1})}$. Similarly, assume there are $N_{1,2}$ effective scatterers around the Rx lying on a ring of radius R_R and the $n_{1,2}$th

978-1-4244-4148-8/09/$25.00 ©2009

This full text paper was peer reviewed at the direction of IEEE Communications Society subject matter experts for publication in the IEEE "GLOBECOM" 2009 proceedings.

$(n_{1,2}=1,...,N_{1,2})$ effective scatterer is denoted by $s^{(n_{1,2})}$. The multiple confocal ellipses model with the Tx and Rx located at the foci represents the TDL structure and has $N_{l,3}$ effective scatterers on the lth ellipse (i.e., lth tap), where $l=1,2,...,L$ with L being the total number of ellipses or taps. The semi-major axis of the lth ellipse and the $n_{l,3}$th ($n_{l,3}=1,...,N_{l,3}$) effective scatterer are denoted by a_l and $s^{(n_{l,3})}$, respectively. The distance between the Tx and Rx is $D=2f$ with f denoting the half length of the distance between the two focal points of ellipses. The antenna element spacings at the Tx and Rx are designated by δ_T and δ_R, respectively. The multi-element antenna tilt angles are denoted by β_T and β_R. The Tx and Rx move with speeds υ_T and υ_R in directions determined by the angles of motion γ_T and γ_R, respectively. The AoA of the wave traveling from an effective scatterer $s^{(n_{1,1})}$, $s^{(n_{1,2})}$, and $s^{(n_{l,3})}$ toward the Rx are denoted by $\phi_R^{(n_{1,1})}$, $\phi_R^{(n_{1,2})}$, and $\phi_R^{(n_{l,3})}$, respectively. The AoD of the wave that impinges on the effective scatterer $s^{(n_{1,1})}$, $s^{(n_{1,2})}$, and $s^{(n_{l,3})}$ are designated by $\phi_T^{(n_{1,1})}$, $\phi_T^{(n_{1,2})}$, and $\phi_T^{(n_{l,3})}$, respectively. Note that ϕ^{LoS} denotes the AoA of a LoS path.

The MIMO fading channel can be described by a matrix $\mathbf{H}(t)=[h_{pq}(t,\tau')]_{M_R\times M_T}$ of size $M_R \times M_T$. According to the TDL concept, the complex impulse response between the pth ($p=1,...,M_T$) Tx, T_p, and the qth ($q=1,...,M_R$) Rx, R_q, can be expressed as $h_{pq}(t,\tau')=\sum_{l=1}^{L} c_l h_{l,pq}(t)\,\delta(\tau'-\tau_l')$ where c_l represents the gain of the lth tap, $h_{l,pq}(t)$ and τ_l' denote the complex time-variant tap coefficient and the discrete propagation delay of the lth tap, respectively. From the above GBSM, the complex tap coefficient for the first tap of the T_p-R_q link is a superposition of the LoS component, single- and double-bounced components, and can be expressed as

$$h_{1,pq}(t)=h_{1,pq}^{LoS}(t)+\sum_{i=1}^{I} h_{1,pq}^{SB_i}(t)+h_{1,pq}^{DB}(t) \tag{1}$$

where

$$h_{1,pq}^{LoS}(t)=\sqrt{\frac{K_{pq}}{K_{pq}+1}}e^{-j2\pi f_c\tau_{pq}} \times e^{j\left[2\pi f_{T_{max}}t\cos\left(\pi-\phi^{LoS}+\gamma_T\right)+2\pi f_{R_{max}}t\cos\left(\phi^{LoS}-\gamma_R\right)\right]} \tag{2a}$$

$$h_{1,pq}^{SB_i}(t)=\sqrt{\frac{\eta_{SB_{1,i}}}{K_{pq}+1}}\lim_{N_{1,i}\to\infty}\sum_{n_{1,i}=1}^{N_{1,i}}\frac{1}{\sqrt{N_{1,i}}}e^{j\left(\psi_{n_{1,i}}-2\pi f_c\tau_{pq,n_{1,i}}\right)} \times e^{j\left[2\pi f_{T_{max}}t\cos\left(\phi_T^{(n_{1,i})}-\gamma_T\right)+2\pi f_{R_{max}}t\cos\left(\phi_R^{(n_{1,i})}-\gamma_R\right)\right]} \tag{2b}$$

$$h_{1,pq}^{DB}(t)=\sqrt{\frac{\eta_{DB_1}}{K_{pq}+1}}\lim_{N_{1,1},N_{1,2}\to\infty}\sum_{n_{1,1},n_{1,2}=1}^{N_{1,1},N_{1,2}}\frac{1}{\sqrt{N_{1,1}N_{1,2}}} \times e^{j\left(\psi_{n_{1,1},n_{1,2}}-2\pi f_c\tau_{pq,n_{1,1},n_{1,2}}\right)} \times e^{j\left[2\pi f_{T_{max}}t\cos\left(\phi_T^{(n_{1,1})}-\gamma_T\right)+2\pi f_{R_{max}}t\cos\left(\phi_R^{(n_{1,2})}-\gamma_R\right)\right]} \tag{2c}$$

Whereas the complex tap coefficient for other taps ($l'>1$) of the T_p-R_q link is a superposition of the single- and double-bounced components, and can be expressed as

$$h_{l',pq}(t)=h_{l',pq}^{SB_3}(t)+h_{l',pq}^{DB_1}(t)+h_{l',pq}^{DB_2}(t) \tag{3}$$

where

$$h_{l',pq}^{SB_3}(t)=\sqrt{\eta_{SB_{l',3}}}\lim_{N_{l',3}\to\infty}\sum_{n_{l',3}=1}^{N_{l',3}}\frac{1}{\sqrt{N_{l',3}}}e^{j\left(\psi_{n_{l',3}}-2\pi f_c\tau_{pq,n_{l',3}}\right)} \times e^{j\left[2\pi f_{T_{max}}t\cos\left(\phi_T^{(n_{l',3})}-\gamma_T\right)+2\pi f_{R_{max}}t\cos\left(\phi_R^{(n_{l',3})}-\gamma_R\right)\right]} \tag{4a}$$

$$h_{l',pq}^{DB_{1(2)}}(t)=\sqrt{\eta_{DB_{l',1(2)}}}\lim_{N_{1,1(2)},N_{l',3}\to\infty}\sum_{n_{1,1(2)},n_{l',3}=1}^{N_{1,1(2)},N_{l',3}}\frac{1}{\sqrt{N_{1,1(2)}N_{l',3}}} \times e^{j2\pi t\left[f_{T_{max}}\cos\left(\phi_T^{(n_{1(l'),1(3)})}-\gamma_T\right)+f_{R_{max}}\cos\left(\phi_R^{(n_{l'(1),3(2)})}-\gamma_R\right)\right]} \times e^{j\left(\psi_{n_{1,1(2)},n_{l',3}}-2\pi f_c\tau_{pq,n_{1,1(2)},n_{l',3}}\right)}. \tag{4b}$$

In (2) and (4), $\tau_{pq}=\varepsilon_{pq}/c$, $\tau_{pq,n_{1,i}}=(\varepsilon_{pn_{1,i}}+\varepsilon_{n_{1,i}q})/c$, $\tau_{pq,n_{1,1},n_{1,2}}=(\varepsilon_{pn_{1,1}}+\varepsilon_{n_{1,1}n_{1,2}}+\varepsilon_{n_{1,2}q})/c$, $\tau_{pq,n_{l',3}}=(\varepsilon_{pn_{l',3}}+\varepsilon_{n_{l',3}q})/c$, and $\tau_{pq,n_{1,1(2)},n_{l',3}}=(\varepsilon_{pn_{1(l'),1(3)}}+\varepsilon_{n_{1(l'),1(3)}n_{l'(1),3(2)}}+\varepsilon_{n_{l'(1),3(2)}q})/c$ are the travel times of the waves through the link T_p–R_q, T_p–$s^{(n_{1,i})}$–R_q, T_p–$s^{(n_{1,1})}$–$s^{(n_{1,2})}$–R_q, T_p–$s^{(n_{l',3})}$–R_q, and T_p–$s^{(n_{1,1})}(s^{(n_{l',3})})$–$s^{(n_{l',3})}(s^{(n_{1,2})})$–$R_q$, respectively, as shown in Fig. 1. Here, c is the speed of light and $I=3$. The symbol K_{pq} designates the Ricean factor. Energy-related parameters $\eta_{SB_{1,i}}$, η_{DB_1} and $\eta_{SB_{l',3}}$, $\eta_{DB_{l',1(2)}}$ specify how much the single-, double-bounced rays contribute to the total scattered power of the first tap and other taps, respectively. Note that these energy-related parameters satisfy $\sum_{i=1}^{I}\eta_{SB_{1,i}}+\eta_{DB_1}=1$ and $\eta_{SB_{l',3}}+\eta_{DB_{l',1}}+\eta_{DB_{l',2}}=1$. The phases $\psi_{n_{1,i}}$, $\psi_{n_{1,1},n_{1,2}}$, $\psi_{n_{l',3}}$, and $\psi_{n_{1,1(2)},n_{l',3}}$ are independent and identically distributed (i.i.d.) random variables with uniform distributions over $[-\pi,\pi)$, $f_{T_{max}}$ and $f_{R_{max}}$ are the maximum Doppler frequencies with respect to the Tx and Rx, respectively.

As presented in [10], the VTD significantly affects statistical properties at all taps of a wideband M2M channel. To take the impact of the VTD into account, we first distinguish between the moving scatterers (cars) around the Tx and Rx, and stationary scatterers located on the roadside, which are represented by a two-ring model and a multiple confocal ellipses model, respectively. For the first tap, the single-bounced rays are generated from the scatterers located on either of the two rings or the first ellipse, while the double-bounced rays are produced from the scatterers located on both rings. This means that the first tap contains a LoS component, a two-ring model with single- and double-bounced rays, and an ellipse model with single-bounced rays, as shown in Fig. 1. For a low VTD, the value of K_{pq} is large since the LoS component can bear a significant amount of power. Also, the received scattered power is mainly from waves reflected by the stationary scatterers located on the ellipse. The moving scatterers located on the two rings are sparse and thus more likely to be single-bounced, rather than double-bounced. This indicates that $\eta_{SB_{1,3}}>\max\{\eta_{SB_{1,1}},\eta_{SB_{1,2}}\}>\eta_{DB_1}$. For a high VTD, the value of K_{pq} is smaller than the one in the low VTD scenario. Also, due to the large amount of moving scatterers, the double-bounced rays of the two-ring model bear more energy than single-bounced rays of two-ring and ellipse models, i.e, $\eta_{DB_1}>\max\{\eta_{SB_{1,1}},\eta_{SB_{1,2}},\eta_{SB_{1,3}}\}$.

For other taps, we assume that the single-bounced rays are generated only from the scatterers located on the corresponding ellipse, while the double-bounced rays are caused by the

978-1-4244-4148-8/09/$25.00 ©2009

scatterers from the combined one ring (either of the two rings) and the corresponding ellipse, as illustrated in Fig. 1. Note that according to the TDL structure, the double-bounced rays in one tap must be smaller in distance than the single-bounced rays on the next ellipse. This is valid only if the condition $\max\{R_T, R_R\} \leq \min\{a_l - a_{l-1}\}$ is fulfilled. For many current M2M channel measurement campaigns, e.g., in [12]–[10], the resolution in delay is 100 ns. Then, the above condition can be modified as $\max\{R_T, R_R\} \leq 15$ m. This indicates that the maximum acceptable width of the road is 30 m, which is sufficiently large to cover most roads in reality. In other words, the proposed wideband model with the specified TDL structure is valid for different scenarios. For a low VTD, the received scattered power is mainly from waves reflected by the stationary scatterers located on the ellipse. This indicates that $\eta_{SB_{l',3}} > \max\{\eta_{DB_{l',1}}, \eta_{DB_{l',2}}\}$. For a high VTD, due to the large amount of moving scatterers, the double-bounced rays from the combined one-ring and ellipse models bear more energy than the single-bounced rays of the ellipse model, i.e, $\min\{\eta_{DB_{l',1}}, \eta_{DB_{l',2}}\} > \eta_{SB_{l',3}}$.

From Fig. 1 and based on the application of the law of cosines in appropriate triangles and the following assumptions $\min\{R_T, R_R, a-f\} \gg \max\{\delta_T, \delta_R\}$ and $D \gg \max\{R_T, R_R\}$, we have

$$\varepsilon_{pq} \approx D - k_p\delta_T\cos\beta_T - k_q\delta_R\cos(\phi^{LoS} - \beta_R) \quad (5a)$$

$$\varepsilon_{pn_{1,1}} \approx R_T - k_p\delta_T\cos(\phi_T^{(n_{1,1})} - \beta_T) \quad (5b)$$

$$\varepsilon_{n_{1,1}q} \approx D - R_T\cos\phi_T^{(n_{1,1})} - k_q\delta_R\cos(\phi_R^{(n_{1,1})} - \beta_R) \quad (5c)$$

$$\varepsilon_{pn_{1,2}} \approx D + R_R\cos\phi_R^{(n_{1,2})} - k_p\delta_T\cos\left(\phi_T^{(n_{1,2})} - \beta_T\right) \quad (5d)$$

$$\varepsilon_{n_{1,2}q} \approx R_R - k_q\delta_R\cos\left(\phi_R^{(n_{1,2})} - \beta_R\right) \quad (5e)$$

$$\varepsilon_{n_{1,1}n_{1,2}} \approx D - R_R\cos\left(\phi_R^{(n_{1,1})} - \phi_R^{(n_{1,2})}\right) \quad (5f)$$

$$\varepsilon_{pn_{l,3}} \approx \xi_T^{(l,3)} - k_p\delta_T\cos\left(\phi_T^{(n_{l,3})} - \beta_T\right) \quad (5g)$$

$$\varepsilon_{n_{l,3}q} \approx \xi_R^{(l,3)} - k_q\delta_R\cos\left(\phi_R^{(n_{l,3})} - \beta_R\right) \quad (5h)$$

$$\varepsilon_{n_{1,1}n_{l',3}} = \sqrt{\left(\xi_T^{(l',3)}\right)^2 + R_T^2 - 2\xi_T^{(l',3)}R_T\cos\left(\phi_T^{(n_{l,1})} - \phi_T^{(n_{l',3})}\right)} \quad (5i)$$

$$\varepsilon_{n_{l',3}n_{1,2}} = \sqrt{\left(\xi_R^{(l',3)}\right)^2 + R_R^2 - 2\xi_R^{(l',3)}R_R\cos\left(\phi_R^{(n_{l,2})} - \phi_R^{(n_{l',3})}\right)} \quad (5j)$$

where $\phi^{LoS} \approx \pi$, $k_p = (M_T - 2p + 1)/2$, $k_q = (M_R - 2q + 1)/2$, $\xi_T^{(n_{l,3})} = \left(a_l^2 + f^2 + 2a_l f\cos\phi_R^{(n_{l,3})}\right) / \left(a_l + f\cos\phi_R^{(n_{l,3})}\right)$, and $\xi_R^{(n_{l,3})} = b_l^2 / \left(a_l + f\cos\phi_R^{(n_{l,3})}\right)$ with b_l denoting the semi-minor axis of the lth ellipse. Note that the AoD $\phi_T^{(n_{1,i})}$, $\phi_T^{(n_{l',3})}$ and AoA $\phi_R^{(n_{1,i})}$, $\phi_R^{(n_{l',3})}$ are independent for double-bounced rays, while are interdependent for single-bounced rays. By using the results in [8], we can express the relationships between the AoD and AoA for the single-bounced two-ring model as $\phi_R^{(n_{1,1})} \approx \pi - \Delta_T\sin\phi_T^{(n_{1,1})}$ and $\phi_T^{(n_{1,2})} \approx \Delta_R\sin\phi_R^{(n_{1,2})}$ with $\Delta_T \approx R_T/D$ and $\Delta_R \approx R_R/D$ and for the multiple confocal ellipses model as $\phi_T^{(n_{l,3})} = \arcsin[b_l^2\sin\phi_R^{(n_{l,3})} / (a_l^2 + f^2 + 2a_l f\cos\phi_R^{(n_{l,3})})]$.

Since the numbers of effective scatterers are assumed to be infinite, i.e., $N_{1,i}, N_{l',3} \to \infty$, the proposed model is actually a mathematical reference model and results in either Ricean PDF (the first tap) or Rayleigh PDF (other taps). For our reference model, the discrete AoD $\phi_T^{(n_{1,i})}$, $\phi_T^{(n_{l',3})}$ and AoA $\phi_R^{(n_{1,i})}$, $\phi_R^{(n_{l',3})}$, can be replaced by continuous random variables $\phi_T^{(1,i)}$, $\phi_T^{(l',3)}$ and $\phi_R^{(1,i)}$, $\phi_R^{(l',3)}$, respectively. Here, we use the von Mises PDF defined as [14] $f(\phi) \triangleq \exp[k\cos(\phi - \mu)] / [2\pi I_0(k)]$ to characterize the AoA and AoD, where $\phi \in [-\pi, \pi)$, $I_0(\cdot)$ is the zeroth-order modified Bessel function of the first kind, $\mu \in [-\pi, \pi)$ accounts for the mean value of the angle ϕ, and k ($k \geq 0$) is a real-valued parameter that controls the angle spread of the angle ϕ. In this paper, for the angle of interest, i.e., the AoD $\phi_T^{(1,1)} \in [-\pi, \pi)$ and AoA $\phi_R^{(1,2)} \in [-\pi, \pi)$ for the two-ring model, and the AoAs $\phi_R^{(l,3)} \in [-\pi, \pi)$ for the multiple confocal ellipse model, we use appropriate parameters (μ and k) of the von Mises PDF as $\mu_T^{(1,1)}$ and $k_T^{(1,1)}$, $\mu_R^{(1,2)}$ and $k_R^{(1,2)}$, and $\mu_R^{(l,3)}$ and $k_R^{(l,3)}$, respectively.

III. ST CF AND SD PSD

In this section, based on the proposed wideband channel model, we will derive the ST CF and the corresponding SD PSD for a non-isotropic scattering environment.

Under the wide-sense stationary uncorrelated-scattering (WSSUS) condition, the correlation properties of two arbitrary channel impulse responses $h_{pq}(t, \tau')$ and $h_{p'q'}(t, \tau')$ of a MIMO M2M channel are completely determined by the correlation properties of $h_{l,pq}(t)$ and $h_{l,p'q'}(t)$ in each tap since no correlations exist between the underlying processes in different taps. Therefore, we can restrict our investigations to the following ST CF $\rho_{h_{l,pq}h_{l,p'q'}}(\tau) = \mathbf{E}\left[h_{l,pq}(t)\, h_{l,p'q'}^*(t-\tau)\right]$, where $(\cdot)^*$ denotes the complex conjugate operation and $\mathbf{E}[\cdot]$ designates the statistical expectation operator. Applying the corresponding von Mises distribution, trigonometric transformations, and the equality $\int_{-\pi}^{\pi} \exp(a\sin c + b\cos c)dc = 2\pi I_0\left(\sqrt{a^2 + b^2}\right)$ [15], and following the similar reasoning in [8], we can obtain the ST CF of the LoS, single-, and double-bounced components as follows.

1) In the case of the LoS component,

$$\rho_{h_{1,pq}^{LoS}h_{1,p'q'}^{LoS}}(\tau) = \sqrt{\frac{K_{pq}K_{p'q'}}{(K_{pq}+1)(K_{p'q'}+1)}}e^{j2\pi G + j2\pi\tau H} \quad (6)$$

where $G = P\cos\beta_T - Q\cos\beta_R$ and $H = f_{T_{max}}\cos\gamma_T - f_{R_{max}}\cos\gamma_R$ with $P = (p' - p)\,\delta_T/\lambda$, $Q = (q' - q)\,\delta_R/\lambda$.

2) In terms of the single-bounce two-ring model

$$\rho_{h_{1,pq}^{SB_{1(2)}}h_{1,p'q'}^{SB_{1(2)}}}(\tau) = \eta_{SB_{1,1(2)}}e^{jC_{T(R)}^{SB_{1(2)}}} \times \frac{I_0\left\{\sqrt{\left(A_{T(R)}^{SB_{1(2)}}\right)^2 + \left(B_{T(R)}^{SB_{1(2)}}\right)^2}\right\}}{\sqrt{(K_{pq}+1)(K_{p'q'}+1)}I_0\left(k_{T(R)}^T\right)} \quad (7)$$

where

978-1-4244-4148-8/09/$25.00 ©2009

$$A_{T(R)}^{SB_{1(2)}}=k_{T(R)}^{(1,1(2))}\cos\mu_{T(R)}^{(1,1(2))}+j2\pi\tau f_{T(R)_{max}}\cos\gamma_{T(R)} +j2\pi P(Q)\cos\beta_{T(R)} \quad (8a)$$

$$B_{T(R)}^{SB_{1(2)}}=k_{T(R)}^{(1,1(2))}\sin\mu_{T(R)}^{(1,1(2))}+j2\pi\tau(f_{T(R)_{max}}\sin\gamma_{T(R)} +f_{R(T)_{max}}\Delta_{T(R)}\sin\gamma_{R(T)})+j2\pi(P(Q)\sin\beta_{T(R)} +Q(P)\Delta_{T(R)}\sin\beta_{R(T)}) \quad (8b)$$

$$C_{T(R)}^{SB_{1(2)}}=-2\pi\tau f_{R(T)_{max}}\cos\gamma_{R(T)}-2\pi Q(P)\cos\beta_{R(T)}. \quad (8c)$$

3) In the case of the single-bounce multiple confocal ellipses model

$$\rho_{h_{l,pq}^{SB_3}h_{l,p'q'}^{SB_3}}(\tau)=\frac{\eta_{SB_{l,3}}}{2\pi I_0\left(k_R^{(l,3)}\right)U} \int_{-\pi}^{\pi}e^{k_R^{(l,3)}\cos\left(\phi_R^{(l,3)}-\mu_R^{(l,3)}\right)}e^{j2\pi\left[P\cos\left(\phi_T^{(l,3)}-\beta_T\right)+Q\cos\left(\phi_R^{(l,3)}-\beta_R\right)\right]} \times e^{j2\pi\tau\left[f_{T_{max}}\cos\left(\phi_T^{(l,3)}-\gamma_T\right)+f_{R_{max}}\cos\left(\phi_R^{(l,3)}-\gamma_R\right)\right]}d\phi_R^{(l,3)} \quad (9)$$

where $\phi_T^{(n_l,3)}=\arcsin[b_l^2\sin\phi_R^{(n_l,3)}/(a_l^2+f^2+2a_lf\cos\phi_R^{(n_l,3)})]$ as mentioned in Section II and $U=\sqrt{(K_{pq}+1)(K_{p'q'}+1)}$ only appears for the first tap.

4) In terms of the double-bounce component for the first tap

$$\rho_{h_{1,pq}^{DB}h_{1,p'q'}^{DB}}(\tau)=\eta_{DB_1} \frac{I_0\left\{\sqrt{\left(A_T^{DB_1}\right)^2+\left(B_T^{DB_1}\right)^2}\right\}I_0\left\{\sqrt{\left(A_R^{DB_1}\right)^2+\left(B_R^{DB_1}\right)^2}\right\}}{\sqrt{(K_{pq}+1)(K_{p'q'}+1)}I_0\left(k_T^{(1,1)}\right)I_0\left(k_R^{(1,2)}\right)} \quad (10)$$

where

$$A_{T(R)}^{DB_1} = k_{T(R)}^{(1,1(2))}\cos\mu_{T(R)}^{(1,1(2))}+j2\pi\tau f_{T(R)_{max}}\cos\gamma_{T(R)} + j2\pi P(Q)\cos\beta_{T(R)} \quad (11a)$$

$$B_{T(R)}^{DB_1} = k_{T(R)}^{(1,1(2))}\sin\mu_{T(R)}^{(1,1(2))}+j2\pi\tau f_{T(R)_{max}}\sin\gamma_{T(R)} + j2\pi P(Q)\sin\beta_{T(R)}. \quad (11b)$$

5) In terms of the double-bounce component for other taps

$$\rho_{h_{l',pq}^{DB_{1(2)}}h_{l',p'q'}^{DB_{1(2)}}}(\tau)=I_0\left\{\sqrt{\left(A_T^{DB_{l',1(2)}}\right)^2+\left(B_T^{DB_{l',1(2)}}\right)^2}\right\} \frac{\eta_{DB_{l',1(2)}}I_0\left\{\sqrt{\left(A_R^{DB_{l',1(2)}}\right)^2+\left(B_R^{DB_{l',1(2)}}\right)^2}\right\}}{I_0\left(k_T^{(1(l'),1(3))}\right)I_0\left(k_R^{(l'(1),3(2))}\right)} \quad (12)$$

where

$$A_T^{DB_{l',1(2)}} = k_T^{(1(l'),1(3))}\cos\mu_T^{(1(l'),1(3))} + j2\pi\tau f_{T_{max}}\cos\gamma_T+j2\pi P\cos\beta_T \quad (13a)$$

$$B_T^{DB_{l',1(2)}} = k_T^{(1(l'),1(3))}\sin\mu_T^{(1(l'),1(3))} + j2\pi\tau f_{T_{max}}\sin\gamma_T+j2\pi P\sin\beta_T \quad (13b)$$

$$A_R^{DB_{l',1(2)}} = k_R^{(l'(1),3(2))}\cos\mu_R^{(1(l'),1(3))} + j2\pi\tau f_{R_{max}}\cos\gamma_R+j2\pi Q\cos\beta_R \quad (13c)$$

$$B_R^{DB_{l',1(2)}} = k_R^{(l'(1),3(2))}\sin\mu_R^{(1(l'),1(3))} + j2\pi\tau f_{R_{max}}\sin\gamma_R+j2\pi Q\sin\beta_R. \quad (13d)$$

Note that since $k_T^{(l',3)}$, $\mu_T^{(l',3)}$ and $k_R^{(l',3)}$, $\mu_R^{(l',3)}$ refer to the same ellipse, $k_T^{(l',3)}=k_R^{(l',3)}$ and $\mu_T^{(l',3)}=\arcsin[b_{l'}^2\sin\mu_R^{(l',3)}/(a_{l'}^2+f^2+2a_{l'}f\cos\mu_R^{(l',3)})]$. Therefore, the ST CF of the channel impulse responses $h_{pq}(t,\tau')$ and $h_{p'q'}(t,\tau')$ can be expressed as $\rho_{pq,p'q'}(\tau)=\sum_{l=0}^{L-1}c_l^2\rho_{l,pq;l,p'q'}(\tau)$.

Applying the Fourier transform to the ST CF $\rho_{h_{l,pq}h_{l,p'q'}}(\tau)$ in terms of τ, we can obtain the corresponding SD PSD as

$$S_{h_{l,pq}h_{l,p'q'}}(f_D)=\int_{-\infty}^{\infty}\rho_{h_{l,pq}h_{l,p'q'}}(\tau)\,e^{-j2\pi f_D\tau}d\tau \quad (14)$$

where f_D is the Doppler frequency. The integral in (14) must be evaluated numerically in the case of the single-bounce multiple confocal ellipses model. While for other cases, by using the equality $\int_0^{\infty}I_0\left(j\alpha\sqrt{x^2+y^2}\right)\cos(\beta x)\,dx = \cos\left(y\sqrt{\alpha^2-\beta^2}\right)/\sqrt{\alpha^2-\beta^2}$ [15] and following the similar reasoning in [8], we can obtain the following closed-form solutions.

1) In the case of the LoS component,

$$S_{h_{1,pq}^{LoS}h_{1,p'q'}^{LoS}}(f_D)=\sqrt{\frac{K_{pq}K_{p'q'}}{(K_{pq}+1)(K_{p'q'}+1)}}e^{j2\pi G}\delta(f_D-H) \quad (15)$$

where $\delta(\cdot)$ denotes the Dirac delta function.

2) In terms of the single-bounce two-ring model

$$S_{h_{1,pq}^{SB_{1(2)}}h_{1,p'q'}^{SB_{1(2)}}}(f_D)=\frac{\eta_{SB_{1,1(2)}}2e^{jU_{T(R)}^{SB_{1(2)}}+j2\pi O_{T(R)}^{SB_{1(2)}}\frac{D_{T(R)}^{SB_{1(2)}}}{W_{T(R)}^{SB_{1(2)}}}}}{\sqrt{(K_{pq}+1)(K_{p'q'}+1)}I_0\left(k_{T(R)}^{(1,1(2))}\right)} \times\frac{\cos\left[\frac{E_{T(R)}^{SB_{1(2)}}}{W_{T(R)}^{SB_{1(2)}}}\sqrt{W_{T(R)}^{SB_{1(2)}}-4\pi^2\left(O_{T(R)}^{SB_{1(2)}}\right)^2}\right]}{\sqrt{W_{T(R)}^{SB_{1(2)}}-4\pi^2\left(O_{T(R)}^{SB_{1(2)}}\right)^2}} \quad (16)$$

where $O_{T(R)}^{SB_{1(2)}}=2\pi\left(f_D\pm f_{R(T)_{max}}\cos\gamma_{R(T)}\right)$, $U_{T(R)}^{SB_{1(2)}}=\mp2\pi Q(P)\cos\beta_{R(T)}$

$$W_{T(R)}^{SB_{1(2)}}=4\pi^2f_{T(R)_{max}}^2+4\pi^2f_{R(T)_{max}}^2\Delta_{T(R)}^2\sin^2\gamma_{R(T)}+8\pi^2 \times f_{T_{max}}f_{R_{max}}\Delta_{T(R)}\sin\gamma_T\sin\gamma_R \quad (17a)$$

$$D_{T(R)}^{SB_{1(2)}}=-j2\pi k_{T(R)}^{(1,1(2))}J_{T(R)}+4\pi^2P(Q)(f_{T(R)_{max}}\cos\left(\beta_{T(R)} -\gamma_{T(R)}\right)+\Delta_{T(R)}f_{R(T)_{max}}\sin\beta_{T(R)}\sin\gamma_{R(T)})+4\pi^2Q(P) \times(\Delta_{T(R)}f_{T(R)_{max}}\sin\beta_{R(T)}\sin\gamma_{T(R)}+\Delta_{T(R)}^2f_{R(T)_{max}} \times\sin\beta_{R(T)}\sin\gamma_{R(T)}) \quad (17b)$$

$$E_{T(R)}^{SB_{1(2)}}=j2\pi k_{T(R)}^{(1,1(2))}(f_{T(R)_{max}}\sin\left(\gamma_{T(R)}-\mu_{T(R)}^{(1,1(2))}\right)+ f_{R(T)_{max}}\Delta_{T(R)}\sin\gamma_{R(T)}\cos\mu_{T(R)}^{(1,1(2))})+4\pi^2P(Q)(f_{T(R)_{max}} \times\sin\left(\beta_{T(R)}-\gamma_{T(R)}\right)-\Delta_{T(R)}f_{R(T)_{max}}\cos\beta_{T(R)}\sin\gamma_{R(T)}) +4\pi^2Q(P)\Delta_{T(R)}f_{T(R)_{max}}\sin\beta_{R(T)}\cos\gamma_{T(R)} \quad (17c)$$

with $J_{T(R)}=f_{T(R)_{max}}\cos\left(\gamma_{T(R)}-\mu_{T(R)}^{(1,1(2))}\right)-f_{R(T)_{max}}\Delta_{T(R)} \times\sin\gamma_{R(T)}\sin\mu_{T(R)}^{(1,1(2))}$. For the Doppler PSD in

978-1-4244-4148-8/09/$25.00 ©2009

(16), the range of Doppler frequency is limited by $\left|f_D \pm f_{R(T)_{max}} \cos\gamma_{R(T)}\right| \leq \sqrt{W_{T(R)}^{SB_{1(2)}}}/(2\pi)$.

3) In terms of the double-bounce component for the first tap

$$S_{h_{1,pq}^{DB} h_{1,p'q'}^{DB}}(f_D) = \frac{\eta_{DB_1}}{\sqrt{(K_{pq}+1)(K_{p'q'}+1)} I_0\left(k_T^{(1,1)}\right)} \times 2e^{j2\pi f \frac{D_T^{DB}}{W_T^{DB}}} \frac{cos\left(\frac{E_T^{DB}}{W_T^{DB}}\sqrt{W_T^{DB}-4\pi^2 f^2}\right)}{I_0\left(k_R^{(1,2)}\right)\sqrt{W_T^{DB}-4\pi^2 f^2}} \odot 2e^{j2\pi f \frac{D_R^{DB}}{W_R^{DB}}} \frac{cos\left(\frac{E_R^{DB}}{W_R^{DB}}\sqrt{W_R^{DB}-4\pi^2 f^2}\right)}{\sqrt{(W_R^{DB}-4\pi^2 f^2}} \quad (18)$$

where $\odot$ denotes convolution, $W_{T(R)}^{DB} = 4\pi^2 f_{T(R)_{max}}^2$

$$D_{T(R)}^{DB} = 4\pi^2 P(Q) f_{T(R)_{max}} \cos\left(\beta_{T(R)} - \gamma_{T(R)}\right) - j2\pi k_{T(R)}^{(1,1(2))} f_{T(R)_{max}} \cos\left(\gamma_{T(R)} - \mu_{T(R)}^{(1,1(2))}\right) \quad (19a)$$

$$E_{T(R)}^{DB} = 4\pi^2 P(Q) f_{T(R)_{max}} \sin\left(\beta_{T(R)} + \gamma_{T(R)}\right) - j2\pi k_{T(R)}^{(1,1(2))} f_{T(R)_{max}} \sin\left(\gamma_{T(R)} - \mu_{T(R)}^{(1,1(2))}\right). \quad (19b)$$

For the Doppler PSD in (18), the range of Doppler frequency is limited by $|f_D| \leq f_{T_{max}} + f_{R_{max}}$.

4) In the case of the double-bounce component for other taps

$$S_{h_{l',pq}^{DB_{1(2)}} h_{l',p'q'}^{DB_{1(2)}}}(f_D) = \frac{\eta_{DB_{l',1(2)}}}{I_0\left(k_T^{(1(l'),1(3))}\right) I_0\left(k_R^{(l'(1),3(2))}\right)} \times 2e^{j2\pi f \frac{D_T^{DB_{l',1(2)}}}{W_T^{DB_{l',1(2)}}}} \frac{cos\left(\frac{E_T^{DB_{l',1(2)}}}{W_T^{DB_{l',1(2)}}}\sqrt{W_T^{DB_{l',1(2)}} - 4\pi^2 f^2}\right)}{\sqrt{W_T^{DB_{l',1(2)}} - 4\pi^2 f^2}} \odot 2e^{j2\pi f \frac{D_R^{DB_{l',1(2)}}}{W_R^{DB_{l',1(2)}}}} \frac{cos\left(\frac{E_R^{DB_{l',1(2)}}}{W_R^{DB_{l',1(2)}}}\sqrt{W_R^{DB_{l',1(2)}} - 4\pi^2 f^2}\right)}{\sqrt{(W_R^{DB_{l',1(2)}} - 4\pi^2 f^2}} \quad (20)$$

where $W_T^{DB_{l',1(2)}} = 4\pi^2 f_{T_{max}}^2$, $W_R^{DB_{l',1(2)}} = 4\pi^2 f_{R_{max}}^2$

$$D_T^{DB_{l',1(2)}} = 4\pi^2 P f_{T_{max}} \cos\left(\beta_T - \gamma_T\right) - j2\pi k_T^{(1(l'),1(3))} f_{T_{max}} \cos\left(\gamma_T - \mu_T^{(1(l'),1(3))}\right) \quad (21a)$$

$$E_T^{DB_{l',1(2)}} = 4\pi^2 P f_{T_{max}} \sin\left(\beta_T - \gamma_T\right) + j2\pi k_T^{(1(l'),1(3))} f_{T_{max}} \sin\left(\gamma_T - \mu_T^{(1(l'),1(3))}\right) \quad (21b)$$

$$D_R^{DB_{l',1(2)}} = 4\pi^2 Q f_{R_{max}} \cos\left(\beta_R - \gamma_R\right) - j2\pi k_R^{(l'(1),3(2))} f_{R_{max}} \cos\left(\gamma_R - \mu_R^{(l'(1),3(2))}\right) \quad (21c)$$

$$E_R^{DB_{l',1(2)}} = 4\pi^2 Q f_{R_{max}} \sin\left(\beta_R - \gamma_R\right) + j2\pi k_R^{(l'(1),3(2))} f_{R_{max}} \sin\left(\gamma_R - \mu_R^{(l'(1),3(2))}\right). \quad (21d)$$

For the Doppler PSD in (20), the range of Doppler frequency is limited by $|f_D| \leq f_{T_{max}} + f_{R_{max}}$. Similar to the ST CF, the SD PSD of the channel impulse responses $h_{pq}(t,\tau')$ and $h_{p'q'}(t,\tau')$ can be expressed as $S_{pq,p'q'}(\tau) = \sum_{l=0}^{L-1} c_l^2 S_{l,pq;l,p'q'}(\tau)$.

IV. Numerical Results and Analysis

In this section, some theoretical statistical properties of the proposed reference model will be given and some of them will be compared with the available measured data in [13].

Figs. 2(a) and (b) show the theoretical SD PSDs of the proposed M2M model for the first tap and second tap, respectively, with different VTDs (low and high) and different antenna separations ($\delta_T = \delta_R = 0$ or $\delta_T = \delta_R = 3\lambda$) when the Tx and Rx move in the same direction. Note that when $\delta_T = \delta_R = 0$, the SD PSDs actually reduce to Doppler PSDs. For comparison purposes, the measured Doppler PSDs taken from Figs. 4 (c) and (d) in [13] are also plotted in Figs. 2(a) and (b), respectively. In [13], the measurement campaigns were performed at a carrier frequency of 5.9 GHz on an expressway with a low VTD. The distance between the Tx and Rx was approximately $D = 300$ m and the directions of movement were $\gamma_T = \gamma_R = 0$ (same direction). Both the Tx and Rx were equipped with one omnidirectional antenna, i.e., SISO case. Based on the measured scenarios in [13], we chose the following environment-related parameters: f_c=5.9 GHz, $f_{T_{max}} = f_{R_{max}}$=570 Hz, D=300 m, a_1=160 m, $a_2 = 180$ m, $R_T = R_R = 10$ m, $k_T^{(1,1)} = 9.6$, $k_R^{(1,2)} = 3.6$, $k_R^{(1,3)} = 11.5$, $k_R^{(2,3)} = 11.7$, $\mu_T^{(1,1)} = 21.7°$, $\mu_R^{(1,2)} = 147.8°$, $\mu_R^{(1,3)} = 171.6°$, and $\mu_R^{(2,3)} = 177.6°$. Using an optimization method and considering the constraints of the Ricean factor and energy-related parameters for different taps as mentioned in Section II, we obtained the following parameters for the two taps with the low VTD: 1) K_{pq}=3.786, η_{DB_1}=0.051, $\eta_{SB_{1,1}}$=0.335, $\eta_{SB_{1,2}}$=0.203, and $\eta_{SB_{1,3}}$=0.411 for Fig. 2(a); 2) $\eta_{DB_{2,1}} = \eta_{DB_{2,2}}$=0.121 and $\eta_{SB_{2,3}}$=0.758 for Fig. 2(b). The excellent agreement between the theoretical and measured Doppler PSDs confirms the utility of the proposed model. The environment-related parameters for the high VTD scenarios are the same as those for low VTD scenarios except $k_T^{(1,1)}$=0.6 and $k_R^{(1,2)}$=1.3, which are related to the distribution of moving scatterers (normally, the smaller values the more distributed moving scatterers, i.e., the higher VTD). The SD PSDs for high VTD shown in Figs. 2(a) and (b) were obtained with the following parameters K_{pq}=0.156, η_{DB_1}=0.685, $\eta_{SB_{1,1}} = \eta_{SB_{1,2}}$=0.126, $\eta_{SB_{1,3}}$=0.063, and $\eta_{DB_{2,1}} = \eta_{DB_{2,2}}$=0.456, $\eta_{SB_{2,3}}$=0.088, respectively. Unfortunately, to the best of the authors' knowledge, no measurement results (e.g., in [12]–[10]) were available regarding the impact of the high VTD (e.g., a traffic jam) on the (space-)Doppler PSD. Comparing the theoretical SD PSDs with different VTDs in Figs. 2 (a) and (b), we observe that the VTD significantly affects the results at different taps in M2M channels. Higher VTDs result in more evenly distributed (space-)Doppler PSDs. Moreover, the space separation results in the fluctuations on SD PSDs.

By using the same parameters as in Figs. 2 (a) and (b), Figs. 3 (a) and (b) depict the corresponding (space-)time CFs for the first tap and second tap, respectively. Again, the VTD

978-1-4244-4148-8/09/$25.00 ©2009

affects greatly the results at different taps. Higher VTDs lead to lower correlation properties.

V. Conclusions

In this paper, we have proposed a wideband MIMO M2M GBSM, which has the ability to study the channel statistics at different time delays and consider the impact of the VTD on channel statistics. From the proposed model, the ST CFs and SD PSDs have been derived. Numerical results have demonstrated that the VTD has a great impact on the resulting CFs and PSDs. Finally, it has been shown that the theoretical Doppler PSDs match very well the measured data, which validates the utility of the proposed model.

Acknowledgements

We acknowledge the support from the Scottish Funding Council for the Joint Research Institute in Signal and Image Processing between the University of Edinburgh and Heriot-Watt University which is a part of the Edinburgh Research Partnership in Engineering and Mathematics (ERPem).

References

[1] C.-X. Wang, X. Cheng, and D. I. Laurenson, "Vehicle-to-vehicle channel modeling and measurements: recent advances and future challenges," *IEEE Commun. Magazine*, accepted for publication.

[2] A. S. Akki and F. Haber, "A statistical model for mobile-to-mobile land communication channel," *IEEE Trans. Veh. Technol.*, vol. 35, no. 1, pp. 2–10, Feb. 1986.

[3] A. S. Akki, "Statistical properties of mobile-to-mobile land communication channels," *IEEE Trans. Veh. Technol.*, vol. 43, no. 4, pp. 826–831, Nov. 1994.

[4] M. Pätzold, B. O. Hogstad, and N. Youssef, "Modeling, analysis, and simulation of MIMO mobile-to-mobile fading channels," *IEEE Trans. Wireless Commun.*, vol. 7, no. 2, pp. 510–520, Feb. 2008.

[5] A. G. Zajić and G. L. Stüber, "Space-time correlated mobile-to-mobile channels: modelling and simulation," *IEEE Trans. Veh. Technol.*, vol. 57, no. 2, pp. 715–726, Mar. 2008.

[6] A. G. Zajić and G. L. Stüber, "Three-dimensional modeling, simulation, and capacity analysis of space-time correlated mobile-to-mobile channels," *IEEE Trans. Veh. Technol.*, vol. 57, no. 4, pp. 2042-2054, July 2008.

[7] X. Cheng, C.-X. Wang, D. I. Laurenson, and A. V. Vasilakos, "Second order statistics of non-isotropic mobile-to-mobile Ricean fading channels," *IEEE ICC'09*, Dresden, Germany, Jun. 2009, pp. 1–5.

[8] X. Cheng, C.-X. Wang, D. I. Laurenson, S. Salous, and A. V. Vasilakos, "An adaptive geometry-based stochastic model for MIMO mobile-to-mobile channels," *IEEE Trans. Wireless Commun.*, vol. 8, no. 9, Sept. 2009.

[9] X. Cheng, C.-X. Wang, D. I. Laurenson, S. Salous, and A. V. Vasilakos, "New deterministic and stochastic simulation models for non-isotropic scattering Mobile-to-mobile Rayleigh fading channels," *Wireless Communications and Mobile Computing Journal*, accepted for publication.

[10] I. Sen and D. W. Matolak, "Vehicle-vehicle channel models for the 5-GHz band," *IEEE Trans. Intell. Transp. Syst.*, vol. 9, no. 2, pp. 235–245, Jun. 2008.

[11] A. G. Zajić and G. L. Stüber, "A three-dimensional parametric model for wideband MIMO mobile-to-mobile channels," *Proc. IEEE GLOBECOM'07*, Washington, DC, USA, Nov. 2007, pp. 3760–3764.

[12] G. Acosta, K. Tokuda, and M. A. Ingram, "Measured joint Doppler-delay power profiles for vehicle-to-vehicle communications at 2.4 GHz," *Proc. IEEE GLOBECOM'04*, Dallas, TX, USA, Nov. 2004, pp. 3813–3817.

[13] G. Acosta and M. A. Ingram, "Six time- and frequency-selective empirical channel models for vehicular wireless LANs," *IEEE Veh. Technol. Mag.*, vol. 2, no. 4, pp. 4–11, Dec. 2007.

[14] A. Abdi, J. A. Barger, and M. Kaveh, "A parametric model for the distribution of the angle of arrival and the associated correlation function and power spectral at the mobile station," *IEEE Trans. Veh. Technol.*, vol. 51, no. 3, pp. 425–434, May 2002.

[15] I. S. Gradshteyn, and I. M. Ryzhik, *Table of Integrals, Series, and Products*. 5th ed, A. Jeffrey, Ed. San Diego, CA: Academic, 1994.

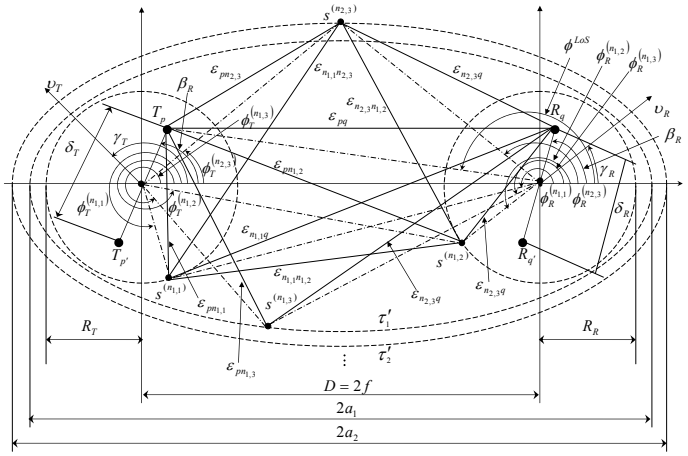

Fig. 1. The proposed wideband GBSM for a MIMO M2M channel.

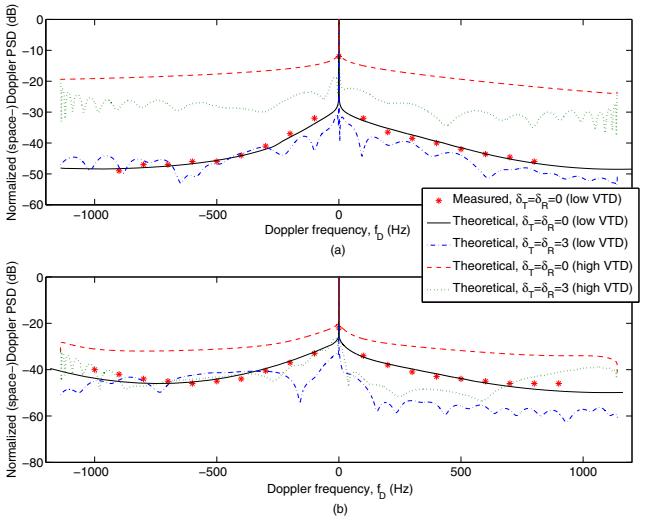

Fig. 2. Normalized (space-)Doppler PSDs of the (a) first tap and (b) second tap of the proposed wideband M2M channel model with low and high VTDs when the Tx and Rx move in the same direction on an expressway.

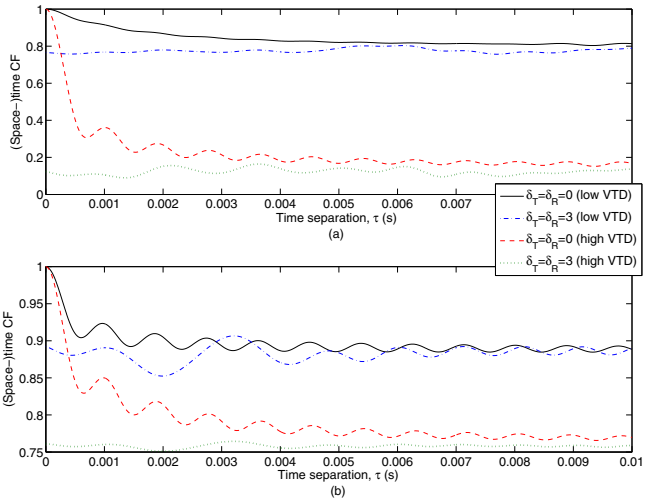

Fig. 3. (Space-)time CFs of the (a) first tap and (b) second tap of the proposed wideband M2M channel model with low and high VTDs when the Tx and Rx move in the same direction on an expressway.

978-1-4244-4148-8/09/$25.00 ©2009